Upper limit on damage zone thickness controlled by seismogenic depth

Jean Paul Ampuero and Xiaolin Mao

Seismological Laboratory, California Institute of Technology, Pasadena, California, USA

Abstract

The thickness of fault damage zones, a characteristic length of the cross-fault distribution of secondary fractures, significantly affects fault stress, earthquake rupture, ground motions and crustal fluid transport. Field observations indicate that damage zone thickness scales with accumulated fault displacement at short displacements, but saturates at few hundred meters for displacements larger than few kilometers. To explain this transition of scaling behavior, we conduct 3D numerical simulations of dynamic rupture with off-fault inelastic deformation on long strike-slip faults. We find that the distribution of coseismic inelastic strain is controlled by the transition from crack-like to pulse-like rupture propagation associated with saturation of the seismogenic depth. The yielding zone reaches its maximum thickness when the rupture becomes a stable pulse-like rupture. Considering fracture mechanics theory, we show that seismogenic depth controls the upper bound of damage zone thickness on mature faults by limiting the efficiency of stress concentration near earthquake rupture fronts. We obtain a quantitative relation between limiting damage zone thickness, background stress, dynamic fault strength, off-fault yield strength and seismogenic depth, which agrees with first-order field observations. Our results help linking dynamic rupture processes with field observations, and contribute to a fundamental understanding of damage zone properties.

Key words: Damage zone; Seismogenic depth; Pulse-like rupture; Fracture; Strike-slip fault

1. Introduction

A typical fault zone architecture comprises a highly deformed core surrounded by a damage zone composed of rocks with higher fracture density and lower elastic moduli than the host rocks. In most mature faults, damage zones are 100 to 400 m wide and have between 20% and 60% wave velocity reductions relative to their host rock [e.g. *Huang and Ampuero,* 2011, and references therein]. Studying the formation of damage zones provides insight into the mechanical, hydraulic and seismic behavior of faults. Fault zone damage is in part inherited from the early process of fracture coalescence and strain localization that led to the formation of the fault, and in part results from damage during earthquakes [*Mitchell and Faulkner,* 2009]. Damage zone thickness, defined as a characteristic scale of the cross-fault distribution of fracture density, varies from a few centimeters on small faults to a few hundred meters on large mature faults. Field observations indicate that damage zone thickness scales linearly with accumulated fault displacement, which is one measure of fault maturity, but saturates at a few hundred meters for fault displacements larger than a few kilometers [*Mitchell and Faulkner*, 2009, 2012; *Savage and Brodsky*, 2011]. Explaining this transition of scaling behavior is the main goal of the present work.

Understanding what controls damage zone thickness is important because this parameter can have significant effects on earthquake rupture, seismic wave radiation, state of stress and hydromechanical properties of the crust. The transition from damage zone to host rock is often sharp, marked by a change of decay rate of fracture density as a function of distance to the fault core [*Johri et al.,* 2014b]. Earthquakes happening inside damage zones can thus generate reflected waves and head waves, which can enhance ground motion near the fault [*Spudich and Olsen*, 2001] but also interact with earthquake ruptures and modulate rupture properties such as

rupture speed, slip rate, and rise time [*Huang et al.*, 2014; *Pelties et al.*, 2014]. In particular, seismological evidence of rupture speeds enhanced by fault zone effects was recently presented by *Huang et al.* [2015] and *Perrin et al.* [2016b]. Damage zones may also alter the stress field surrounding faults, leading to mean stress increase and stress rotations, thereby allowing high pore fluid pressure weakening of unfavorably oriented faults [*Faulkner et al.*, 2006]. The effect of reduced elastic moduli in damage zones and their systematic changes along strike induced by fault growth help explain patterns of long-term fault displacement and earthquake slip distributions [*Cappa et al.*, 2014; *Perrin et al.*, 2016b]. Damage zone thickness is also an important factor affecting the fluid transport and storage properties of the crust and reservoirs [*Johri et al.*, 2014b].

Off-fault inelastic deformation is observed all along the rupture trace of large earthquakes [e.g., *Milliner et al.*, 2015], demonstrating the importance of damage generated coseismically in the vicinity of propagating rupture fronts. Off-fault yielding during dynamic rupture propagation has been previously studied through analytical approaches [*Poliakov et al.*, 2002; *Rice et al.*, 2005] and numerical simulations with off-fault plasticity [e.g., *Andrews*, 1976a, 2005; *Gabriel et al.*, 2013] or continuum damage [*Xu et al.*, 2014]. Plastic strain is often discussed as a proxy for damage [e.g., *Xu et al.*, 2012a, b] and can be mapped into fracture density for comparison with field observations [*Johri et al.*, 2014a]. The thickness of the off-fault yielding zone generated by a single self-similar rupture (crack-like or pulse-like) increases linearly with distance from the hypocenter [*Andrews*, 2005; *Gabriel et al.*, 2013]. In contrast, the yielding zone thickness generated by steady-state pulse-like ruptures remains constant [*Ben-Zion and Shi*, 2005; *Ben-Zion and Ampuero*, 2009; *Xu et al.*, 2012a, b]. The accumulated effect of multiple slip events can be considered as a superposition of the coseismic plastic strain fields of each individual slip

event [*Johri et al.*, 2014a]. Most previous numerical studies of coseismic damage are based on 2D models or on 3D models of relatively short ruptures [*Ma and Andrews*, 2010], and are unable to consider the influence of the aspect ratio of a rupture, i.e. the ratio of its along-strike length to along-dip width. A notable exception are the 3D simulations of long ruptures by *Shi and Day* [2013], which yielded an eventually stable thickness of the off-fault plastic zone. As proposed by *Day* [1982] on the basis of an asymptotic analysis of stress concentration near a 3D rupture front, the inelastic deformation induced by a rupture with high aspect ratio is controlled by width rather than length.

In this study, we use 3D numerical simulations of dynamic rupture on strike-slip faults with large aspect ratios to study first-order aspects of the off-fault yielding pattern in long faults. In particular, we assess the role of seismogenic depth in limiting fault zone thickness. The ingredients of our model, described in Section 2, are intentionally minimalistic: material properties surrounding the fault are uniform, a linear slip-weakening friction law is assumed on the fault. In Section 3, comparing results of simulations with different seismogenic depths, we find that the distribution of inelastic strain is controlled by the transition from crack-like to pulse-like rupture propagation associated with saturation of the seismogenic depth. The yielding zone reaches its maximum thickness when the rupture becomes a stable pulse-like rupture. In Section 4 we develop quantitative insight, from the perspective of fracture mechanics, on how the transition to pulse-like rupture in long faults explains the saturation of damage zone thickness with accumulated fault displacement. In particular, we show that seismogenic depth controls the upper limit of damage zone thickness on mature faults. In Section 5 we discuss how our results help linking dynamic rupture models with field observations, and contribute to a fundamental understanding of damage zone properties.

2. Model description

The geometry of our numerical model is shown in Fig. 1 (a). The fault is long enough (along strike) for dynamic rupture to reach an approximately steady state after it reaches the surface and bottom boundaries of the fault (Figs. 2 and 3 (a)). The simulation domain is large enough to avoid boundary effects. We aim to demonstrate the influence of seismogenic depth (W) on rupture propagation and inelastic response near advancing rupture fronts. Therefore, we consider a single, vertical and planar strike-slip fault embedded in a uniform material with P-wave velocity of 6 km/s, S-wave velocity of 3.464 km/s and density of 2670 kg/m^3.

The initial stress field is depth-dependent, and fluid pressure is hydrostatic and time-independent. The directions of principal stresses are shown in Fig. 1 (a) and the initial effective normal stress and shear stress on the fault in Figs. 1 (b) and (c), respectively, for the case with W = 15 km. To avoid a sudden arrest of rupture at depth, the deviatoric components of stress are linearly tapered to zero from 12 km to 15 km depth and the normal stress increases up to the same value as the effective intermediate principal stress.

A linear slip-weakening friction law [*Andrews*, 1976] is employed, in which the friction coefficient μ is a function of cumulative slip D:

$$\mu(D) = \mu_s - (\mu_s - \mu_d) \min(D/D_c, 1), \quad (1)$$

where μ_d is the dynamic friction coefficient, μ_s is the static friction coefficient, and D_c is the critical slip-weakening distance. Here, we assume μ_s = 0.6, μ_d = 0.1 (representative of thermally weakened faults) and D_c = 0.3 m (representative of seismological estimates for large earthquakes). The fault strength τ includes a cohesion C_o (different from off-fault plastic cohesion C, which will be discussed later):

$$\tau = C_o + \mu(\sigma_n - P_f), \quad (2)$$

where σ_n is normal stress on the fault, and P_f is fluid pressure. To avoid an excessively intense surface break of the rupture, C_o is set to 0.4 MPa at depths larger than 3 km, and linearly increases to 4 MPa from 3 km depth to the surface (Figs. 1(b) and 1(c)). The relative strength S parameter [*Andrews*, 1976; *Das and Aki*, 1977], defined by

$$S = \frac{\tau_s - \tau_0}{\tau_0 - \tau_d} \quad (3)$$

where τ_0, $\tau_s = \mu_s \sigma_0$, $\tau_d = \mu_d \sigma_0$ and σ_0 are initial shear stress, static strength, dynamic strength and initial normal stress, respectively, is set to 2 on most of the fault (Fig. 1(c)).

Rupture initiation is achieved by forcing the fault to rupture within a circular zone surrounding the hypocenter (Fig. 1(b)). We linearly reduce the friction coefficient from its static value at specified time T to its dynamic value within a time period t_o = 0.5 s. T is set to be infinity outside the nucleation zone, and inside the nucleation zone

$$T = \frac{r}{0.7V_S} + \frac{0.081 r_{crit}}{0.7V_S}\left(\frac{1}{1-(\frac{r}{r_{crit}})^2} - 1\right), \quad (4)$$

where r is the distance from the hypocenter, r_{crit} is the radius of the nucleation zone (set to 3 km here) and V_S is shear wave velocity. This procedure forces the rupture to expand at a variable speed, about $0.7V_S$ near the hypocenter and decreasing to zero at r_{crit}. Spontaneous rupture gradually overtakes the ever-slowing forced rupture.

The Drucker-Prager yield criterion [*Drucker and Prager*, 1952] is adopted in our study as the off-fault yielding criterion, by which the yield stress $Y(\boldsymbol{\sigma})$ depends on the mean normal stress:

$$Y(\boldsymbol{\sigma}) = -(\sigma_{kk}/3 + P_f)\sin\varphi + C\cos\varphi, \quad (5)$$

where $\boldsymbol{\sigma}$ is the stress tensor, φ is the internal frictional angle and C is the plastic cohesion. The maximum shear stress is

$$\tau_{max} = \sqrt{\frac{1}{2}s_{ij}s_{ij}}, \quad (6)$$

where $\boldsymbol{s}$ is the deviatoric part of the stress tensor

$$s_{ij} = \sigma_{ij} - \frac{1}{3}\sigma_{kk}\delta_{ij} \ . \quad (7)$$

A Drucker-Prager yield function is defined as:

$$F(\boldsymbol{\sigma}) = \tau_{max} - Y(\boldsymbol{\sigma}), \quad (8)$$

with yielding starting when $F(\boldsymbol{\sigma}) = 0$. After yielding starts, the Duvaut-Lions-type viscoplasticity [e.g. *Duan and Day*, 2008] is used to calculate the accumulation of plastic strain $\boldsymbol{\varepsilon}^p$ through:

$$\dot{\varepsilon}_{ij} = \frac{1}{2\mu T_v} F(\sigma) \frac{s_{ij}}{\tau_{max}} , \quad (9)$$

where μ is shear modulus and T_v is the viscoplastic relaxation time scale. Viscosity is included here as an artificial means to mitigate mesh-dependency due to extreme strain localization [*Templeton and Rice*, 2008]. A scalar quantity is defined to describe the magnitude of plastic strain (Figs. 4 and 5) as:

$$\epsilon_0^p = \sqrt{2\epsilon_{ij}^p \epsilon_{ij}^p} . \quad (10)$$

In this study φ = arctan(0.6), C = 1.36 MPa and T_v = 0.03 s.

The 3D dynamic rupture problem coupled to wave propagation and plastic deformation is solved numerically with SPECFEM3D, a code based on the spectral element method [*Kaneko et al.*, 2008; *Galvez et al.*, 2014]. The implementation of viscoplasticity in SPECFEM3D was verified by comparison to other numerical methods in a community benchmark problem [*Harris et al.*, 2011].

3. Simulation results

3.1 Crack- to pulse-like rupture transition controlled by fault geometry

Seismic observations and dynamic rupture models indicate that rise time, the duration of earthquake slip at a given point on a fault, can be either comparable to or much shorter than the

overall earthquake duration. The former case defines crack-like ruptures [*Madariaga*, 1976] while the latter case corresponds to pulse-like ruptures [*Heaton*, 1990]. Proposed mechanisms of local slip arrest leading to pulse-like ruptures include self-healing due to velocity-dependent friction [e.g., *Perrin et al.*, 1995; *Beeler and Tullis*, 1996] and stopping phases (healing fronts) generated by spatial changes of initial stress or strength on the fault [e.g., *Beroza and Mikumo*, 1996]. A particular case of the latter mechanism, first described by *Day* [1982], is the generation of stopping phases at the deep limit of the seismogenic zone, which acts as a rupture barrier.

On mature strike-slip faults, the fault length is usually much larger than the fault width, as in the model setup described in Fig. 1 (a). Our first example of dynamic rupture simulation with off-fault plasticity is on a long fault with W = 15 km. We show resulting snapshots of slip rate in Fig. 2, and slip rate and slip profiles at 7.5 km depth in Figs. 3 (a) and (b), respectively. The rupture first grows as a self-similar crack-like rupture: the rupture front expands in all directions from the hypocenter, the peak slip rate increases with rupture propagation distance, and slip occurs simultaneously within the whole ruptured region. When the rupture front reaches the bottom boundary of the seismogenic zone, a stopping front is generated and propagates back into the ruptured area. When the healing front reaches the surface, the rupture splits into two pulses (i.e. a pair of rupture fronts followed closely by healing fronts) that propagate in separate directions along the fault strike. The pulses eventually reach a steady state, characterized by stable slip, rupture speed and peak slip velocity. Notably, the steady pulse width (i.e. the along-strike length of the region of active slip at a given time) is comparable to the seismogenic width W (Fig. 3 (a)).

3.2 Plastic strain distribution

Figure 4 shows horizontal and vertical plastic strain distributions of our model with W = 15 km. Similar to *Johri et al*. [2014a], we observe that plastic strain decays as a function of distance from the fault core as a power-law at short distance, and drops more abruptly, exponentially at larger distance (Fig. 5). In this simulation and in those presented in the next section the change of plastic strain decay behavior occurs near $\varepsilon_p = 10^{-3.3}$. Hence, to facilitate the comparison between all our simulations, we define the thickness of the damage zone, H, as the distance at which $\varepsilon_p = 10^{-3.3}$. In the presence of dilatancy (volumetric and deviatoric plastic strains are proportional) and assuming the average fracture aperture is spatially uniform, fracture density is proportional to ε_p [*Johri et al.,* 2014a]. This relation connects rupture models with plasticity to field studies, in which the definition of damage zone thickness is based on fracture density. Field data on fracture density vs. distance has been interpreted either as power laws [e.g. *Savage and Brodsky*, 2011] or as exponential [*Mitchell and Faulkner,* 2009], but to our knowledge a transition between these two decay behaviors has not been reported. The field data shown in Figure 7-a of *Savage and Brodsky* [2011] is a rare example reminiscent of such transition. Nevertheless, based on the theoretical arguments developed in section 4, we expect the scaling properties discussed in this work to hold also for other definitions of H.

In Fig. 4 (a), along the fault, the thickness of the damage zone first grows with increasing rupture distance, as found in 2D models [e.g. *Gabriel et al.,* 2013; *Xu et al.,* 2012b]. However, H saturates at distances over ~ 50 km, where the rupture becomes a stable pulse. This saturation was also noted in 3D simulations by *Shi and Day* [2013]. In the deep region, damage is limited to the extensional quadrants. In Fig. 4 (b), the vertical plastic strain pattern shows a “flower-like” structure with a narrow damage zone of nearly constant thickness in the deeper region and a wide damage zone of increasing thickness near the surface. Similar flower-like patterns of plastic

strain were observed in previous 3D simulations [*Ma and Andrews*, 2010]. In the shallower region, the inelastic strain is induced by seismic waves ahead of the rupture front, and is distributed in both extensional and compressional regions. The constant H in the deeper region in our model is explained in section 5 as a result of a linear depth-distribution of both initial stress and strength.

3.3 Damage zone thickness comparison for different seismogenic depths

We now examine the effect of the seismogenic depth W on the damage zone thickness H at mid-seismogenic depth. We conduct four additional simulations in which all settings are the same as in the previous one except the seismogenic depth, which is taken as W = 9, 12, 18 and 21 km, respectively. The width of the stress tapering zone near the fault bottom and the width of the zone of increased fault cohesion near the surface are set proportional to W.

In Fig. 6 we compare the plastic strain distributions resulting from the three simulations with $W \leq 15$ km. The plastic strain patterns are similar for the three models. In particular, they all eventually reach a steady damage zone geometry at sufficient distance from the hypocenter. However, the off-fault extent of their plastic zones is different, it increases as a function of W. Fig. 5 compares fault-normal profiles of plastic strain at 5 km depth and at a horizontal distance of 70 km from the hypocenter, a distance at which the damage zone has already reached a steady thickness, H_{max}, in all five simulations. In this figure, distance is normalized by W and the inset shows how our measure of damage zone thickness H (the distance from the fault at which plastic strain is $\varepsilon_p = 10^{-3.3}$) depends on W. The steady damage zone thicknesses in our five models vary from ~100 to ~500 meters, a range of values that agrees well with the largest values obtained from field observations [*Savage and Brodsky*, 2011]. The approximate collapse in Fig. 5 of the

normalized plastic strain profiles corresponding to the four models with $W \geq 12$ km indicates that H_{max} is approximately proportional to W if W is large enough. The dark gray line in the inset of Fig. 5 is a hypothesized asymptotic linear $H_{max} - W$ scaling. The model with the smallest W (9 km) has an H_{max} significantly over-predicted by the linear $H_{max} - W$ scaling (Fig. 5 inset). These key results of our simulations are put on a theoretical basis in the next section.

4. Theoretical estimate of damage zone thickness

On the basis of fracture mechanics arguments, *Ben-Zion and Ampuero* [2009] and *Xu et al.* [2012b] developed theoretical relations between the thickness of dynamically generated damage zones, initial stresses, material strength and rupture speed. *Xu et al.* [2012b] found that this approach predicts well the yielding zone thickness obtained in 2D dynamic crack-like rupture simulations with off-fault plasticity. A fracture mechanics analysis of damage zones formed by quasi-static fault growth was developed by *Scholz et al.* [1993]. These models predict a self-similar scaling in which H is proportional to fault or rupture length L, without saturation. Here, we apply the dynamic fracture mechanics approach to pulse-like ruptures in 3D, which allows us to assess the effect of seismogenic width.

An estimate of the thickness of the damage zone generated by a dynamic rupture is the distance at which the stress concentration near the rupture tip exceeds the yield strength of the material (e.g. equation 14a of *Ben-Zion and Ampuero* [2009]):

$$H \approx \left(\frac{K}{\tau_s - \tau_0}\right)^2 \qquad (11)$$

where K is the dynamic stress intensity factor. The yield strength τ_s involved in this equation pertains to the off-fault material, and can be higher than the yield strength of the fault. This estimate assumes that the on-fault slip-weakening zone near the rupture front is much smaller than the rupture dimensions, which is the case in our simulations, and significantly smaller than H, which is better satisfied at large W as discussed at the end of this section. The squared stress intensity factor K^2 scales with a characteristic length of the rupture. For small earthquakes, represented as circular ruptures, the characteristic length is the rupture radius and Equation (11) predicts self-similar scaling between H and rupture length L. For larger earthquakes with elongated rupture area, $L \gg W$, the characteristic length that controls K is the shortest one [e.g., *Eshelby*, 1957], hence H scales with rupture width W. For pulse-like ruptures, the characteristic length is the along-strike width of the pulse. As illustrated in section 3.1, large earthquake ruptures that saturate the seismogenic depth are inevitably pulse-like, and their pulse width scales with seismogenic depth W. This break in self-similarity leads to a linear relation between H and W, as found in our simulations with large W (inset of Fig. 5).

In more detail, following *Xu et al.* [2012b] but considering pulse-like ruptures and ignoring some factors of order one,

$$H \approx \left(k(v_r)\frac{\tau_0-\tau_d}{\tau_s-\tau_d}\right)^2 W \qquad (12)$$

where k is a decreasing dimensionless function of rupture speed, v_r. In particular, k and K are larger at the stopping ends of a rupture, especially if arrest occurs in a fault region with large fracture energy rather than low initial stress. Moreover, pulse width can be smaller than in our simulations if the pulse-like behavior is controlled by self-healing due to dynamic weakening mechanisms [*Heaton*, 1990] instead of a geometric effect of the finite seismogenic depth. Hence an upper bound on coseismic damage zone thickness is

$$H_{max} \approx \left(\frac{\tau_0 - \tau_d}{\tau_s - \tau_d}\right)^2 W \qquad (13)$$

This linear $H_{max} - W$ relation is consistent with our simulation results at large W (Fig. 5 inset, dashed gray line). Equations (12) and (13) should be understood as containing a multiplicative factor of order 1 that accommodates different definitions of *H* and encapsulates geometric effects ignored in our derivation. For instance, free surface effects can contribute a factor 2, resulting from the effective doubling of W by a mirror-image rupture.

The departure from a linear $H_{max} - W$ scaling at low W in our simulations (Fig. 5 inset) is attributed here to a blunting effect of the on-fault slip-weakening zone. The derivation of Equation (13) assumes that H_{max} is significantly larger than the slip-weakening zone size ℓ_c. Using equation 24 of *Gabriel et al.* [2013], we find that the ratio H_{max}/ℓ_c is proportional to a function of rupture speed and, more importantly, to the non-dimensional number κ introduced by *Madariaga and Olsen* [2000] to represent the ratio between available elastic energy and fracture energy:

$$\kappa = W(\tau_0 - \sigma_0\mu_d)^2 / G\sigma_0(\mu_s - \mu_d)D_c \qquad (14)$$

where G is shear modulus. Because the initial stresses τ_0 and σ_0 increase linearly with depth in our models, κ is proportional to W^2 and decreasing W rapidly decreases κ. We thus consider that the model with W = 9 km has approached an unusual regime associated with low values of H_{max}/ℓ_c in which the smoothening effect of the slip-weakening zone reduces significantly the off-fault stresses and hence the damage zone thickness. This is simply an artifact of the large value of critical slip-weakening distance (D_c) and low value of initial stress ratio τ_0/σ_0 adopted here to limit the computational cost of the simulations. We expect that simulations with smaller κ should give a nearly linear $H_{max} - W$ relation down to smaller values of *W*. Moreover, regardless of the value of κ, Equation (13) provides a useful upper bound on H_{max}.

5. Discussion and conclusions

Our 3D dynamic rupture simulations and fracture mechanics arguments indicate that damage zone thickness is ultimately bounded in long faults by the limiting effect of seismogenic depth on the efficiency of stress concentration near a rupture front. In particular, Equation (13) provides a quantitative prediction of the relation between limiting damage zone thickness, state of stress, dynamic fault strength, off-fault yield strength and seismogenic depth, which we can compare to field observations.

Average stress drops ($\tau_0 - \tau_d$) of large earthquakes are typically on the order of a few MPa, an order of magnitude smaller than estimates of strength drop ($\tau_s - \tau_d = \sigma_0(\mu_s - \mu_d)$) based on typical values of effective confining stress σ_0 at seismogenic depth and of static and dynamic friction coefficients. Hence, the predicted H_{max} is about two orders of magnitude smaller than W, that is, a few 100 m. This order-of-magnitude estimate is consistent with field observations of damage zone thickness on large-displacement faults [*Savage and Brodsky*, 2011; *Mitchell and Faulkner*, 2009, 2012].

The saturation of H as a function of fault displacement (long-term cumulative slip) in the data compiled by *Savage and Brodsky* [2011] occurs at displacements of a few km or less. Considering that displacement to fault length ratios typically range from 0.1 to 0.01 on faults with displacement shorter than a few km [*Kim and Sanderson*, 2005], the saturation of H starts at fault lengths ranging from a few 10 km to a few 100 km. This range encompasses the typical values of seismogenic depth, which is consistent with our model. In particular, in the data of strike-slip faults compiled by *Kim and Sanderson* [2005], a displacement of a few km

corresponds to a length of a few 10 km, which quantitatively supports our interpretation of the role of seismogenic depth in limiting damage zone thickness.

The constant thickness of deep damage zones found in our simulations can be rationalized from a theoretical basis. Our model assumed linearly increasing initial shear stress and material strength, such that the ratio $(\tau_0 - \tau_d)/(\tau_s - \tau_d)$ is independent of depth. Equation 13 predicts a constant H in this situation. This estimate is not appropriate near the surface, where dynamic free surface effects and cohesion play important roles. Damage zone properties at seismogenic depth are difficult to resolve by seismological techniques. Current field data compilations [e.g., *Savage and Brodsky*, 2011] include observations on exhumed faults that capture fault zone structures from a range of depths, including shallow and deep ones, which may contribute to the data scatter. In this study, we have focused on a scaling feature (saturation of H) that is apparent in the field data despite its significant scatter.

Our theoretical argument further suggests that the ratio H_{max}/W is a relative measure of the stress τ_0 at which an active fault operates in the long term. In particular, Equation 13 predicts that a critically stressed fault, in which the average shear stress is close to yield ($\tau_0 \approx \tau_s$), would have a thicker damage zone than a fault operating at sub-critical stress. According to this model, the small value of H_{max}/W in natural faults is additional evidence that long mature faults operate at stresses significantly lower than the crustal yield strength.

The simulations presented here are intentionally based on simplifying assumptions regarding fault friction, fault geometry, state of stress and material heterogeneities. An important next step in the development of earthquake models is to study the evolution of fault zone damage through multiple earthquake cycles on long faults, including not only the accumulation of plastic strain but also the reduction in elastic moduli around the fault [*Kaneko et al.*, 2011; *Xu et al.*, 2014]. If

346 the evolution of a fault towards increasing maturity is accompanied by a tendency to operate at
347 lower stress [*Fang and Dunham*, 2013], our theoretical results suggest the hypothesis that further
348 damage may localize on thinner zones, which could be tested in simulations of long-term
349 damage evolution. Such a simulation framework could also provide insight on how fault growth
350 leaves systematic changes of damage zone properties along strike that may control the
351 distribution of earthquake slip and rupture speed [*Cappa et al.*, 2014; *Perrin et al.*, 2016b].

352 An additional argument allows us to conclude that short-term damage processes are essential in
353 the evolution of fault zone structure. While the present work emphasizes damage occurring over
354 co-seismic time scales, a similar saturation of damage zone thickness is predicted for slower,
355 quasi-static damage processes, because the static stress intensity factor K is also limited by the
356 depth extent of fault slip (seismic or aseismic). However, if damage were dominated by time
357 scales longer than deep afterslip and longer than the relaxation time of the asthenosphere, the
358 relevant model would be a throughgoing crack in a thin elastic slab (the lithosphere, decoupled
359 from the asthenosphere). The long-term K would no longer be limited by W, as shown by *Lehner*
360 *et al.* [1981], and the damage zone thickness would not saturate.

361 These different predictions of scaling behavior also help us identify aspects of fault zone
362 evolution that may be controlled by long-term damage processes. At a larger scale than the
363 damage zones considered here, faults develop an "outer damage zone" [*Perrin et al.*, 2016b] that
364 encompasses a network of secondary faults. The younger fault branches often organize near the
365 tips of the main fault into splay fault fans, whose width scales with fault length without
366 saturation [*Perrin et al.*, 2016a]. This observation is consistent with a model in which the
367 evolution of outer damage zones is controlled by fault growth and branching processes operating
368 over time scales longer than the viscous relaxation time of the asthenosphere.

Acknowledgments

This work was supported by the Southern California Earthquake Center (funded by NSF Cooperative Agreement EAR-1033462 and USGS Cooperative Agreement G12AC20038) and by the National Science Foundation (CAREER award EAR-1151926). We thank Yoshihiro Kaneko for sharing his version of the SPECFEM3D code modified for the SCEC TPV27 benchmark, and Steve Day and an anonymous reviewer for their stimulating comments.

References

Andrews, D. J. (1976a), Rupture propagation with finite stress in antiplane strain, *J. Geophys. Res.*, 81 (20), 3575-3582.

Andrews, D. J. (1976b), Rupture velocity of plane strain shear cracks, *J. Geophys. Res.*, *81(32)*, 5679–5687, doi:10.1029/JB081i032p05679.

Andrews, D. J. (2005), Rupture dynamics with energy loss outside the slip zone, *J. Geophys. Res.*, *110*, B01307, doi:10.1029/2004JB003191.

Beeler, N. M., and T. E. Tullis (1996), Self-healing slip pulses in dynamic rupture models due to velocity-dependent strength, *Bull. Seismol. Soc. Am.*, *86(4)*, 1130–1148.

Ben-Zion, Y., and J.-P. Ampuero (2009), Seismic radiation from regions sustaining material damage, *Geophys. J. Int.*, *178(3)*, 1351-1356, doi: 10.1111/j.1365-246X.2009.04285.x.

Ben-Zion, Y., and Z. Shi (2005), Dynamic rupture on a material interface with spontaneous generation of plastic strain in the bulk, *Earth Planet. Sci. Lett.*, *236*, 486–496, doi:10.1016/j.epsl.2005.03.025.

Beroza, G. C., and T. Mikumo (1996), Short slip duration in dynamic rupture in the presence of heterogeneous fault properties, *J. Geophys. Res., 101(B10),* 22,449–22,460, doi:10.1029/96JB02291.

Cappa, F., Perrin, C., Manighetti, I., Delor, E. (2014), Off--fault long-term damage: A condition to account for generic, triangular earthquake slip profiles, *Geochem. Geophys. Geosys*., 15, 1476–1493, doi:10.1002/2013GC005182.

Das, S., and K. Aki (1977), A numerical study of two-dimensional spontaneous rupture propagation, *Geophys. J. R. Astron. Soc., 50(3),* 643–668, doi.10.1111/j.1365-246X.1977.tb01339.x.

Day, S. M. (1982), Three-dimensional finite difference simulation of fault dynamics: Rectangular faults with fixed rupture velocity, *Bull. Seismol. Soc. Am., 72(3),* 705–727.

Drucker, D. C., and W. Prager (1952), Soil mechanics and plastic analysis or limit design, *Q. Appl. Math., 10,* 157–165.

Duan, B., and S. M. Day (2008), Inelastic strain distribution and seismic radiation from rupture of a fault kink, *J. Geophys. Res., 113,* B12311, doi:10.1029/2008JB005847.

Eshelby, J. D. (1957), The determination of the elastic field of an elliptical inclusion, and related problems, *Proc. R. Soc. London, 241,* 376–396.

Fang, Z. and E. M. Dunham (2013), Additional shear resistance from fault roughness and stress levels on geometrically complex faults, *J. Geophys. Res.*, **118**(7), 3642-3654, doi:10.1002/jgrb.50262

Faulkner, D. R., T. M. Mitchell, D. Healy, and M. J. Heap (2006), Slip on 'weak' faults by the rotation of regional stress in the fracture damage zone, *Nature, 444,* 922-925, doi:10.1038/nature05353.

Gabriel, A. A., J. P. Ampuero, L. A. Dalguer and P. M. Mai (2013), Source properties of dynamic rupture pulses with off-fault plasticity, *J. Geophys. Res.*, 118 (8), 4117-4126, doi:10.1002/jgrb.50213.

Galvez, P., J. P. Ampuero, L. A. Dalguer, S. N. Somala and T. F. Nissen-Meyer (2014), Dynamic earthquake rupture modelled with an unstructured 3-D spectral element method applied to the 2011 M9 Tohoku earthquake, *Geophys. J. Int.*, 198 (2), 1222-1240, doi:10.1093/gji/ggu203.

Harris, R. A., et al. (2011), Verifying a computational method for predicting extreme ground motion, *Seis. Res. Let*., 82 (5), 638-644, doi:10.1785/gssrl.82.5.638

Heaton, T. H. (1990), Evidence for and implications of self-healing pulses of slip in earthquake rupture, *Phys. Earth Planet. Inter.*, *64(1)*, 1–20.

Huang, Y., and J. P. Ampuero (2011), Pulse-like ruptures induced by low-velocity fault zones, *J. Geophys. Res.*, *116*, B12307, doi:10.1029/2011JB008684.

Huang, Y., J. P. Ampuero, and D. V. Helmberger (2014), Earthquake ruptures modulated by waves in damaged fault zones, *J. Geophys. Res. Solid Earth*, *119*, 3133–3154, doi:10.1002/2013JB010724.

Huang, Y., J. P. Ampuero and D. V. Helmberger (2015), The potential for supershear earthquakes in damaged fault zones - Theory and observations, *Earth Planet. Sci. Lett.*, *433*, 109-115, doi:10.1016/j.epsl.2015.10.046.

Johri, M., E. M. Dunham, M. D. Zoback, and Z. Fang (2014a), Predicting fault damage zones by modeling dynamic rupture propagation and comparison with field observations, *J. Geophys. Res. Solid Earth*, *119*, 1251–1272, doi:10.1002/2013JB010335.

437 Johri, M., M. D. Zoback, and P. Hennings (2014b). A scaling law to characterize fault-
438 damage zones at reservoir depths, *AAPG Bull., 98(10),* 2057-2079.
439 Kaneko, Y., N. Lapusta and J. P. Ampuero (2008), Spectral-element modeling of spontaneous
440 earthquake rupture on rate and state faults: Effect of velocity-strengthening friction at shallow
441 depths, *J. Geophys. Res*., 113 (B9), B09317, doi:10.1029/2007JB005553.
442 Kaneko, Y., J. P. Ampuero and N. Lapusta (2011), Spectral-element simulations of long-term
443 fault slip: Effect of low-rigidity layers on earthquake-cycle dynamics, *J. Geophys. Res.*, 116,
444 B10313, doi:10.1029/2011JB008395.
445 Lehner, F. K., V. C. Li, and J. R. Rice (1981), Stress diffusion along rupturing plate
446 boundaries, *J. Geophys. Res., 86(B7),* 6155–6169, doi:10.1029/JB086iB07p06155.
447 Ma, S., and D. J. Andrews (2010), Inelastic off-fault response and three-dimensional
448 dynamics of earthquake rupture on a strike-slip fault, *J. Geophys. Res., 115*, B04304,
449 doi:10.1029/2009JB006382.
450 Madariaga, R. (1976), Dynamics of an expanding circular fault, *Bull. Seismol. Soc. Am.*,
451 *66(3),* 639–666.
452 Madariaga, R., and K. B. Olsen (2000), Criticality of rupture dynamics in 3-D, *Pure Appl.*
453 *Geophys*., *157 (11-12),* 1981-2001.
454 Milliner, C. W., Dolan, J. F., Hollingsworth, J., Leprince, S., Ayoub, F., & Sammis, C.
455 (2015), Quantifying near-field and off-fault deformation patterns of the 1992 Mw 7.3 Landers
456 earthquake, *Geochem. Geophys. Geosyst., 16 (5),* 1577-1598, doi:10.1002/2014GC005693.
457 Mitchell, T. M., and D. R. Faulkner (2009), The nature and origin of off-fault damage
458 surrounding strike-slip fault zones with a wide range of displacements: A field study from the

459 Atacama fault system, northern Chile, *J. Struct. Geol.*, *31*, 802–816,
460 doi:10.1016/j.jsg.2009.05.002.

461 Mitchell, T. M., and D. R. Faulkner (2012), Towards quantifying the matrix permeability of
462 fault damage zones in low porosity rocks, *Earth Planet. Sci. Lett., 339-340,* 24-31.

463 Perrin, G., J. R. Rice, and G. Zheng (1995), Self-healing slip pulse on a frictional surface, *J.*
464 *Mech. Phys. Solids, 43(9),* 1461–1495.

465 Perrin, C., I. Manighetti, and Y. Gaudemer (2016a), Off-fault tip splay networks: A genetic
466 and generic property of faults indicative of their long-term propagation, *C. R. Geosci., 348*, 52–
467 60, doi:10.1016/j.crte.2015.05.002.

468 Perrin, C., I. Manighetti, J. P. Ampuero, F. Cappa and Y. Gaudemer (2016b), Location of
469 largest earthquake slip and fast rupture controlled by along-strike change in fault structural
470 maturity due to fault growth, *J. Geophys. Res., 121 (5),* 3666-3685, doi:10.1002/2015JB012671.

471 Pelties, C., Y. Huang and J. P. Ampuero (2014), Pulse-like rupture induced by three-
472 dimensional fault zone flower structures, *Pure Appl. Geophys.*, 172 (5), 1229–1241,
473 doi:10.1007/s00024-014-0881-0.

474 Poliakov, A. N., R. Dmowska and J. R. Rice (2002), Dynamic shear rupture interactions with
475 fault bends and off-axis secondary faulting, *J. Geophys. Res.*, 107 (B11), ESE-6.

476 Rice, J. R., C. G. Sammis and R. Parsons (2005), Off-fault secondary failure induced by a
477 dynamic slip pulse, *Bull. Seismo. Soc. Am.*, 95 (1), 109-134.

478 Savage, H. M., and E. E. Brodsky (2011), Collateral damage: Evolution with displacement of
479 fracture distribution and secondary fault strands in fault damage zones, *J. Geophys. Res., 116*,
480 B03405, doi:10.1029/2010JB007665.

Scholz, C. H., N. H. Dawers, J. Z. Yu, M. H. Anders, and P. A. Cowie (1993), Fault growth and fault scaling laws: preliminary results. *J. Geophys. Res., 98 (B12)*, 21951-21961.

Shi, Z., and S. M. Day (2013), Rupture dynamics and ground motion from 3-D rough-fault simulations, *J. Geophys. Res., 118*, 1122–1141, doi:10.1002/jgrb.50094.

Spudich, P., and K. Olsen (2001), Fault zone amplified waves as a possible seismic hazard along the Calaveras fault in central California, *Geophys. Res. Lett.*, 28 (13), 2533–2536, doi:10.1029/2000GL011902.

Templeton, E. L., and J. R. Rice (2008), Off-fault plasticity and earthquake rupture dynamics: 1. Dry materials or neglect of fluid pressure changes, *J. Geophys. Res.*, 113 (B9), B09306, doi:10.1029/2007JB005529.

Xu, S., Y. Ben-Zion, and J. P. Ampuero (2012a), Properties of inelastic yielding zones generated by in-plane dynamic ruptures-I. Model description and basic results, *Geophys. J. Int., 191(3)*, 1325–1342, doi:10.1111/j.1365-246X.2012.05679.x.

Xu, S., Y. Ben-Zion, and J. P. Ampuero (2012b), Properties of inelastic yielding zones generated by in-plane dynamic ruptures-II. Detailed parameter-space study, *Geophys. J. Int., 191(3)*, 1343-1360, doi:10.1111/j.1365-246X.2012.05685.x.

Xu, S., Y. Ben-Zion, J. P. Ampuero and V. Lyakhovsky (2014), Dynamic ruptures on a frictional interface with off-fault brittle damage: Feedback mechanisms and effects on slip and near-fault motion, *Pure Appl. Geophys.*, 172 (5), 1243-1267, doi:10.1007/s00024-014-0923-7.

Figure captions

Fig.1 Model setup. (a) Model geometry and background stresses. σ_1 and σ_3 are maximum and minimum principal initial stresses, respectively. The angle between σ_1 and the fault strike is 30.96^o and the intermediate principal stress is vertical. The seismogenic zone depth is denoted by *W*. (b) Fault plane view showing the nucleation zone (circle), a shallow zone of increased cohesion and a deep zone of tapered stresses. (c) Initial stresses and frictional strength on the fault as a function of depth.

Fig.2 Development of a steady pulse-like rupture on a long fault. Distribution of horizontal slip rate at six different times (indicated by labels on the top left of each panel) in a dynamic rupture simulation with seismogenic depth W = 15 km.

Fig.3 Slip rate (a) and slip (b) profiles every 2.5 s from 1.25 s to 26.25 s at 7.5 km depth for the rupture model with W = 15 km.

Fig.4 Distribution of plastic strain (ε_p) for the model with W = 15 km: (a) horizontal distribution at 5 km depth and (b) vertical distribution along the cross-section shown by a green dashed line in (a). The label C indicates a compressional region, and T a tensional region.

Fig.5 Plastic strain (ε_p) as a function of distance from the fault plane for models with different seismogenic depths (W) ranging from 9 to 21 km. Profiles are located at 5 km depth and 70 km horizontal distance from the hypocenter. The inset shows with crosses the damage zone thickness (H), defined here as the distance at which $\varepsilon_p = 10^{-3.3}$, as a function of W for all simulations. The solid gray curve is our interpretation of the non-linear trend in the simulation data. The dashed

gray line is an asymptotic linear relation between H and W at large W motivated by our theoretical analysis.

Fig.6 Comparison of the plastic strain distributions among different models with W= 9, 12 and 15 km, respectively, (a) along a vertical cross-section at 70 km horizontal distance from the hypocenter and (b) on a horizontal cross-section at 5 km depth.

(a)

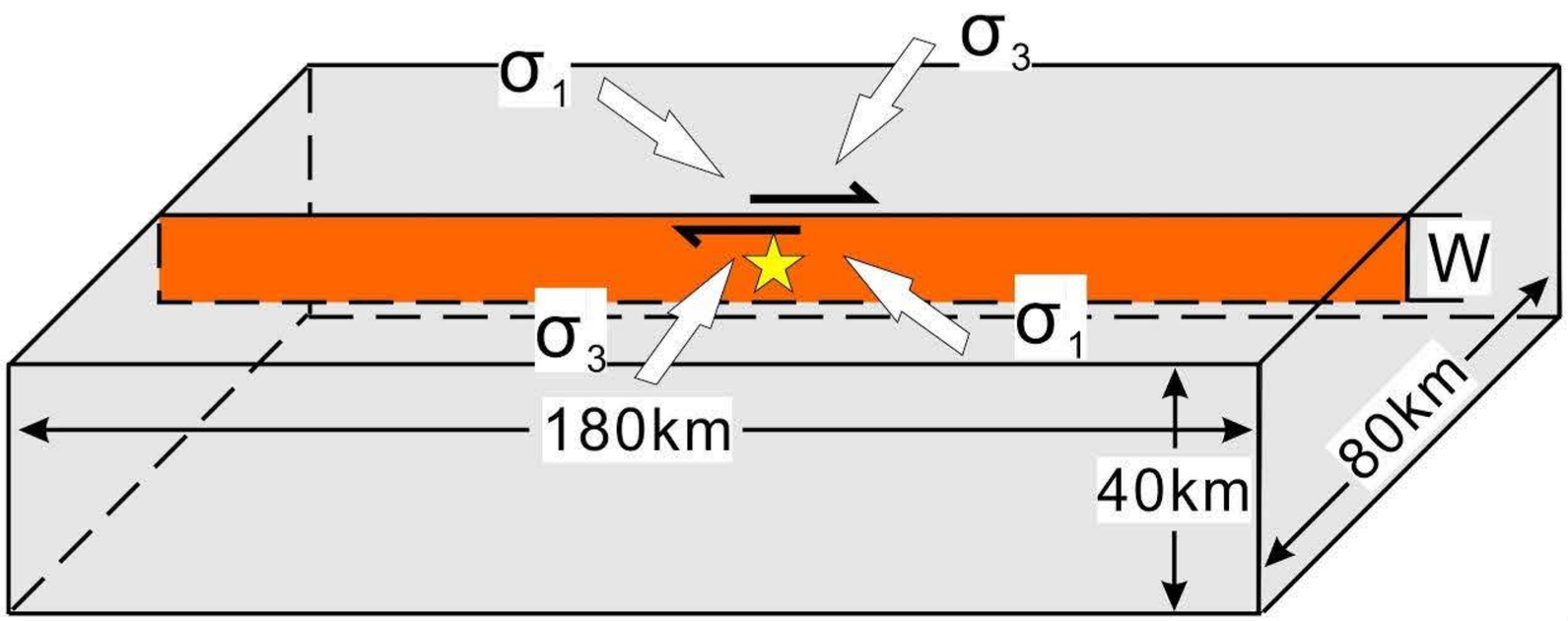
σ1
σ3
W
σ3
σ1
180km
40km
80km

(b)

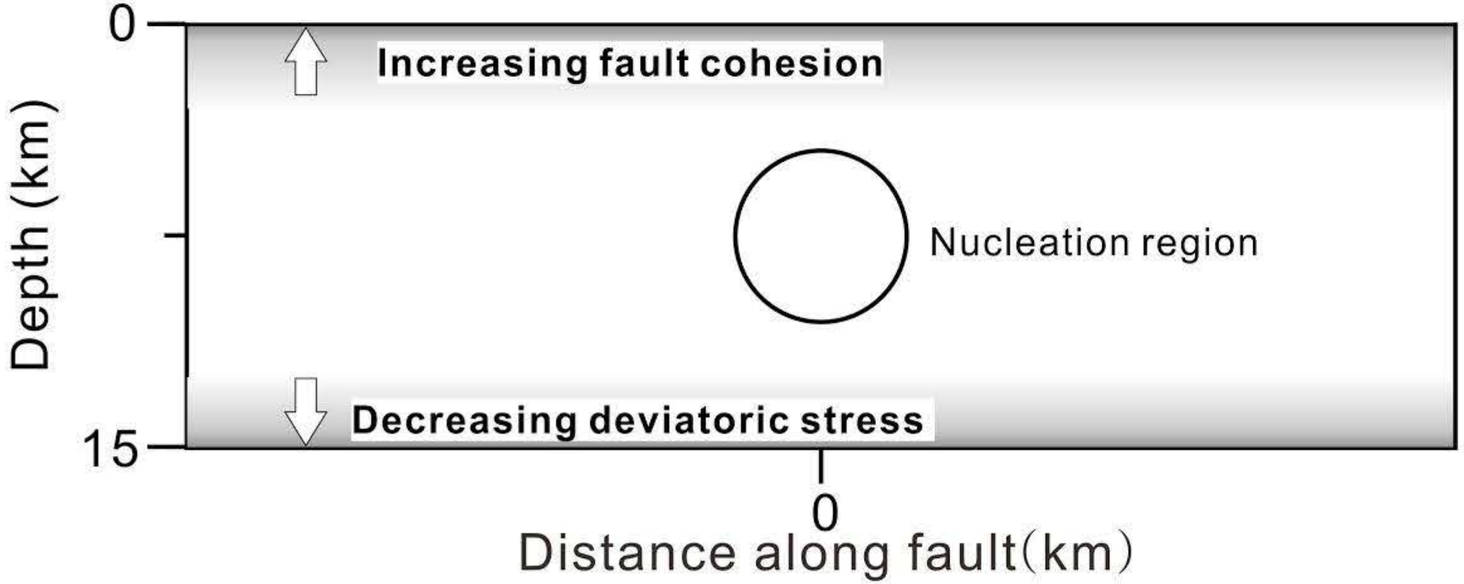
0
Increasing fault cohesion
Nucleation region
Decreasing deviatoric stress
15
Depth (km)
0
Distance along fault(km)

(c)

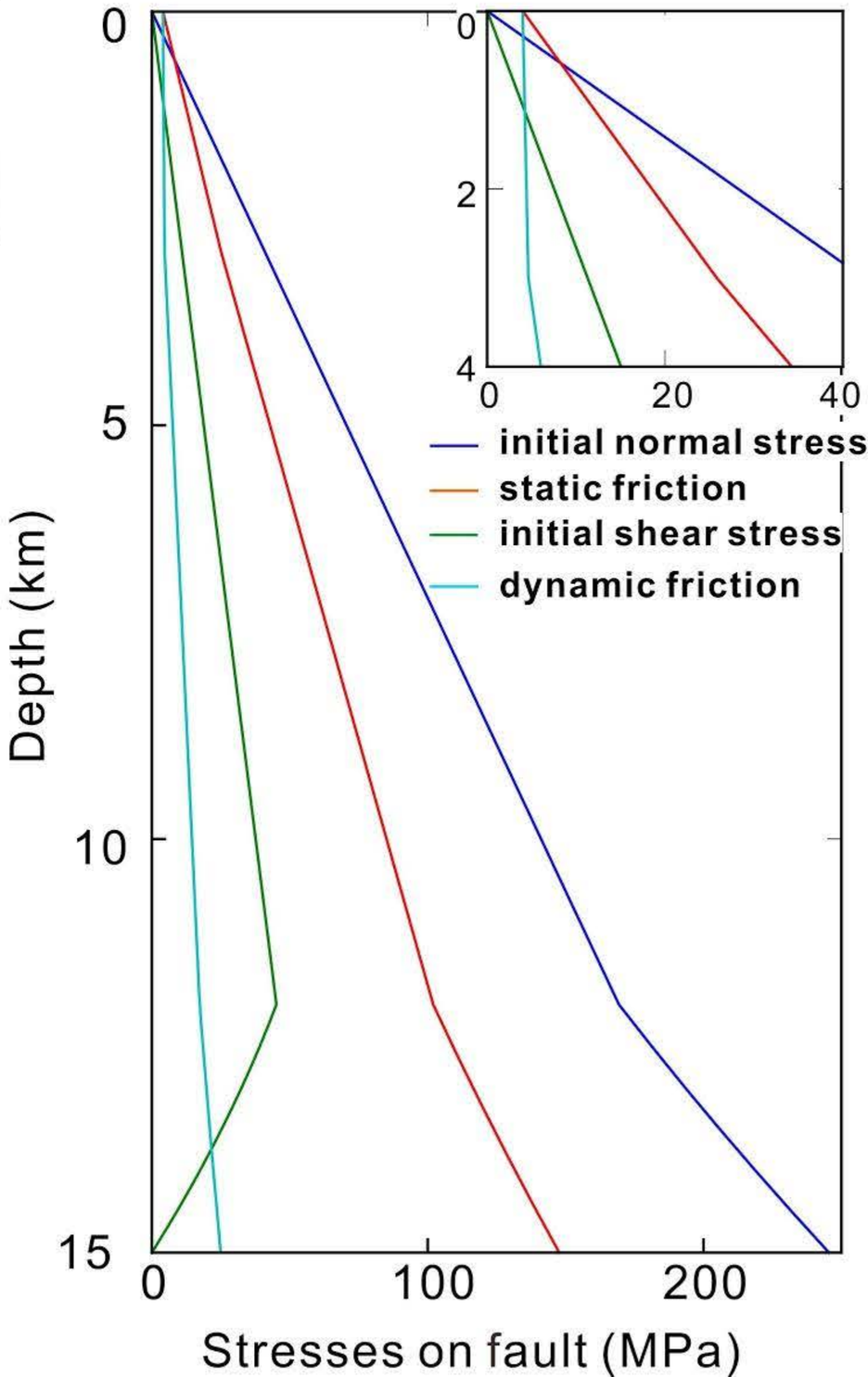
0
5
10
15
Depth (km)
0
100
200
Stresses on fault (MPa)
0
2
4
0
20
40
initial normal stress
static friction
initial shear stress
dynamic friction

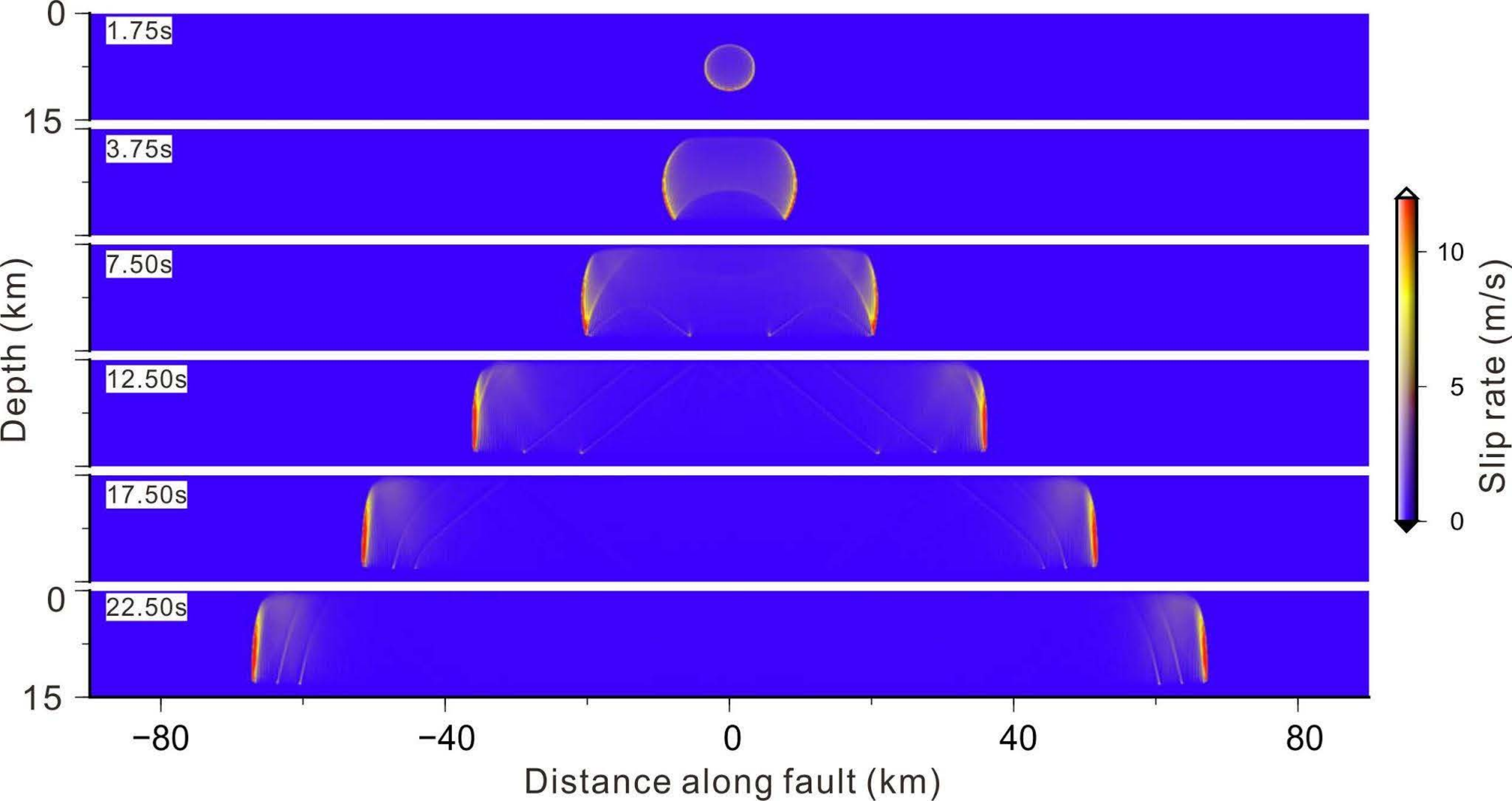
1.75s
3.75s
7.50s
12.50s
17.50s
22.50s
0
15
0
15
Depth (km)
−80
−40
0
40
80
Distance along fault (km)
10
5
0
Slip rate (m/s)

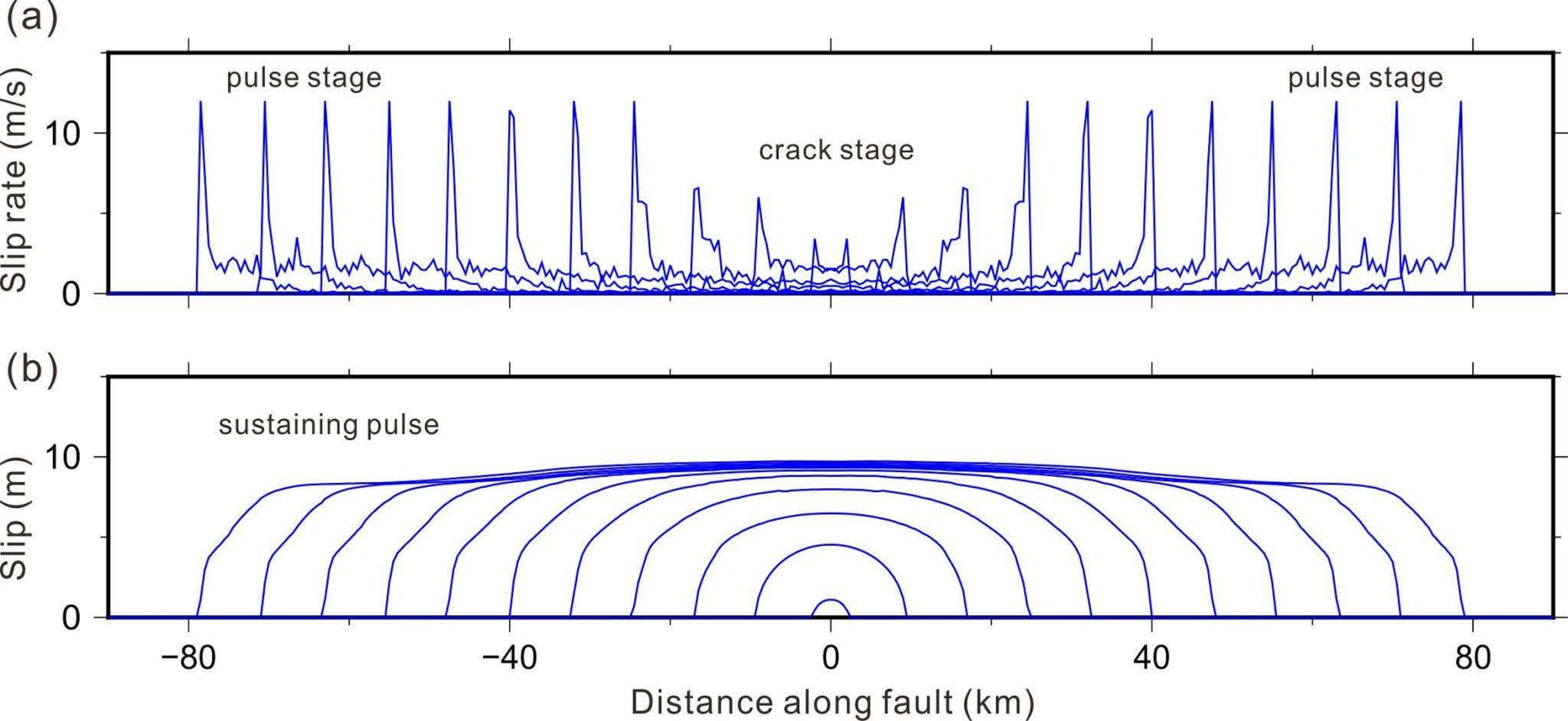
(a)
pulse stage
crack stage
pulse stage
Slip rate (m/s)
10
0
(b)
sustaining pulse
Slip (m)
10
0
−80
−40
0
40
80
Distance along fault (km)

(a)

800
400
0
-400
-800

Distance perpendicular to fault(m)

5km depth

"T"
"C"
fault
"C"
"T"
(b)

−80
−40
0
40
80

Distance along fault(km)

−3.0
−2.5
−2.0

$\log_{10}(\varepsilon_p)$

(b)

0
4
8
12

depth (km)

fault
"C"
"T"

-1000
0
1000

Distance perpendicular to fault(m)

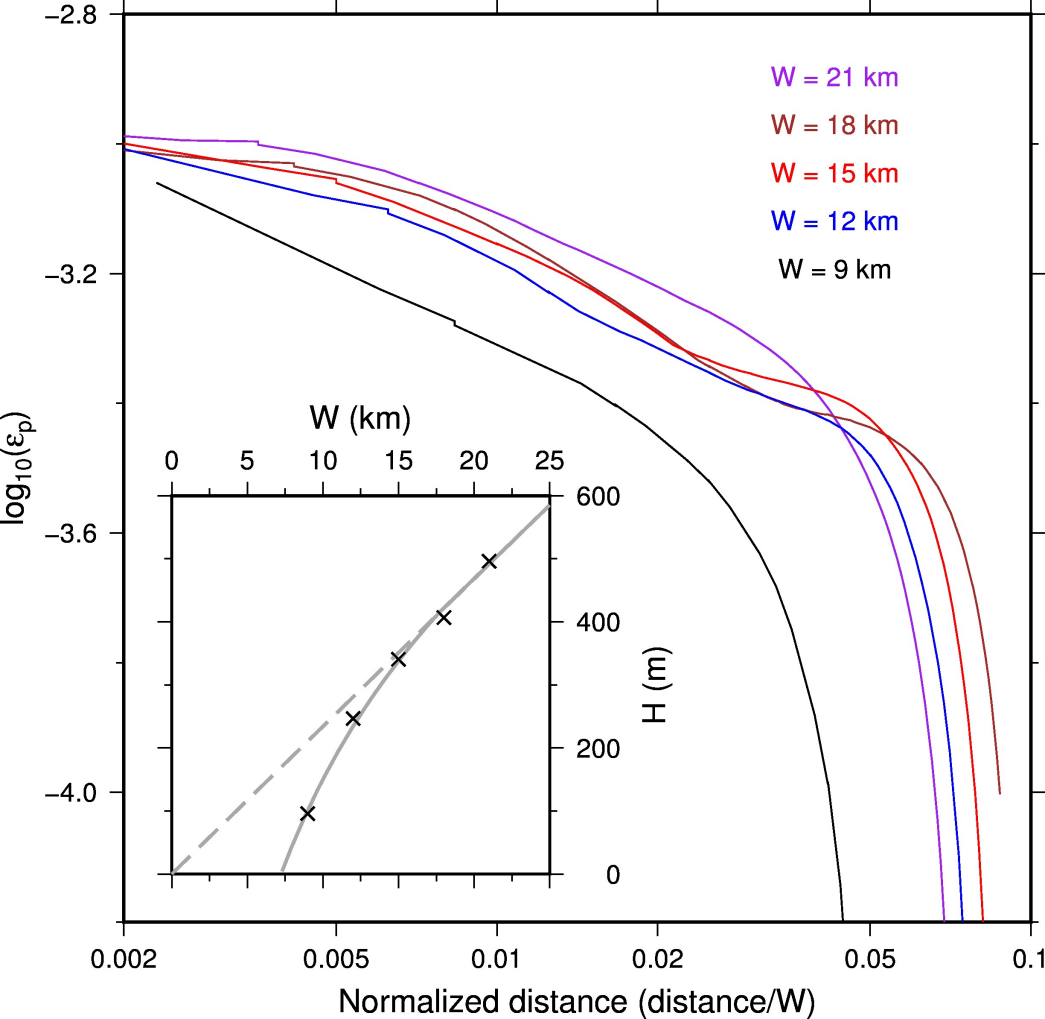
W = 21 km
W = 18 km
W = 15 km
W = 12 km
W = 9 km
log10(εp)
−2.8
−3.2
−3.6
−4.0
0.002
0.005
0.01
0.02
0.05
0.1
Normalized distance (distance/W)
W (km)
0
5
10
15
20
25
H (m)
600
400
200
0

(a)

W = 9 km

W = 12 km

W = 15 km

0

4

8

12

depth (km)

fault

(b)

"C"

"T"

-1000

0

1000

-100

Distance perpendicular to fault(m)

−3.0

−2.5

−2.0

$\log_{10}(\varepsilon_p)$

(b)

W = 15 km

W = 12 km

W = 9 km

800

400

0

-400

-800

fault

Distance perpendicular to fault(m)

−80

−40

40

80

Distance along fault(km)